Materials Today Physics 11 (2019) 100171

Contents lists available at ScienceDirect

Materials Today Physics

journal homepage: https://www.journals.elsevier.com/materials-today-physics

# Extremely space and time restricted thermal transport in the high temperature *Cmcm* phase of thermoelectric SnSe

C.-H. Lee [a], M.-H. Ma [a], W.-H. Li [a, *], P.-C. Wei [b], Y.-Y. Chen [b], Y. Zhao [c], J.W. Lynn [d]

[a] Department of Physics, National Central University, Jhongli, 32001, Taiwan
[b] Institute of Physics, Academia Sinica, Taipei, 11529, Taiwan
[c] Department of Materials Science and Engineering, University of Maryland, College Park, MD, 20742, USA
[d] NIST Center for Neutron Research, National Institute of Standards and Technology, Gaithersburg, MD, 20899, USA

ARTICLE INFO

*Article history:*
Received 30 October 2019
Received in revised form
29 November 2019
Accepted 5 December 2019
Available online 17 December 2019

*Keywords:*
Thermoelectric
Phonon dispersion
Neutron scattering
Phonon lifetime

ABSTRACT

Phonon dispersions and linewidths of layered thermoelectric SnSe in the high temperature *Cmcm* phase have been mapped by inelastic neutron scattering measurements. Downturns in the phonon dispersion reveal soft phonon energies at larger wave vectors for phonon modes propagating in the crystallographic basal *a*-*c* plane. The downturns can be described by a $q^2$-dependency, indicative of the appearance of strong electron-phonon scattering in the *Cmcm* phase. A $q^3$-dependency is also needed for a satisfactory description of the dispersions, revealing the existence of a huge lattice anharmonicity. Group velocities of the transverse acoustic phonons are reduced by as much as 37% through the structural phase transition at 798 K. The scattering of phonons is so strong that they propagation only over a few unit cells in length, with the lifetime as short as ~0.3 ps. The very short phonon lifetimes and very limited phonon propagation length, together with negative phonon group velocity at large wavevectors restricts heat transport at high temperatures. Our results reveal the origin of the extremely low thermal conductivity of SnSe in the *Cmcm* phase.



## 1. Introduction

Materials that facilitate a direct conversion of thermal energy into electrical energy are valuable for the development of new resources for power generation. The key factors for effective thermoelectric performance are a low thermal conductivity together with a high electron mobility. The dimensionless quantity *ZT* (where *Z* is the thermoelectric figure-of-merit and *T* the absolute temperature) is used to mark the efficiency in heat-to-electricity conversion. The key physical parameters affecting *Z* include the Seebeck coefficient *S*, electrical conductivity σ, and thermal conductivity κ, defining $Z \equiv S^2\sigma/\kappa$ [1–5]. The discovery of surprisingly low thermal conductivity that gives a record-high ZT in SnSe and in hole/electron-doped SnSe [6–13] has attracted a great deal of attention both to use these materials in applications and to understand its origin and further improve performance. SnSe is a p-type semiconductor, with an energy gap of 0.86 eV and a high optical absorption coefficient. It crystallizes into a two-atom-thick layered orthorhombic *Pnma* structure at room temperature, where each Sn ion is surrounded by 7 coordination Se ions with three short and four very long Sn–Se bonds arranged in a highly distorted interconnected $SnSe_7$ polyhedral configuration [6,14–18]. We mark the two-atom-thick layer as the crystallographic basal *a*-*c* plane that is stacked along the axial *b*-axis direction. Thermal displacement of the Sn ions drives SnSe to undergo a structural relaxation to a higher-symmetry orthorhombic *Cmcm* phase above ~800 K (Fig. 1(a)).

In the *Pnma* phase, the ZT of SnSe increases with increasing temperature, reaching a record-high maximum of 2.6 at 923 K in the *Cmcm* phase [6]. The high *ZT* of SnSe links directly to the ultra-low thermal conductivity [6,19,20]. It has been demonstrated that the giant phonon anharmonicity from the lattice instability generates temperature-dependent force constants, which give rise to the ultra-low values and thermally decreasing thermal conductivity in the *Pnma* phase [21–23]. All three key parameters of *S*, σ and κ become nearly temperature independent in the high temperature *Cmcm* phase [6,24]. The large decrease in the thermal reduction rate of *S* helps to preserve the high figure-of-merit in the *Cmcm* phase, where the thermally activated electrons for conduction have been saturated. First-principles lattice dynamics calculations have

* Corresponding author.
*E-mail address:* whli@phy.ncu.edu.tw (W.-H. Li).

https://doi.org/10.1016/j.mtphys.2019.100171
2542-5293/

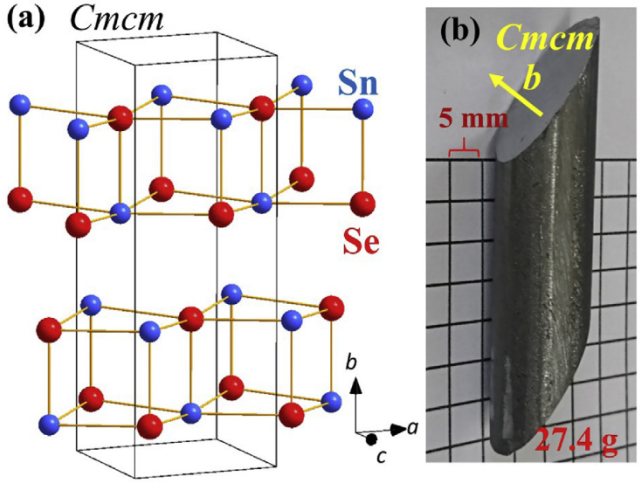


**Fig. 1. Crystal structure and the single crystal sample.** (a) Crystal structure of SnSe in the high temperature *Cmcm* phase. (b) Photo image of the SnSe single crystal used in this study. The crystal weighed 27.4 g, where the flat surface indicates the basal *a*-*c* plane.

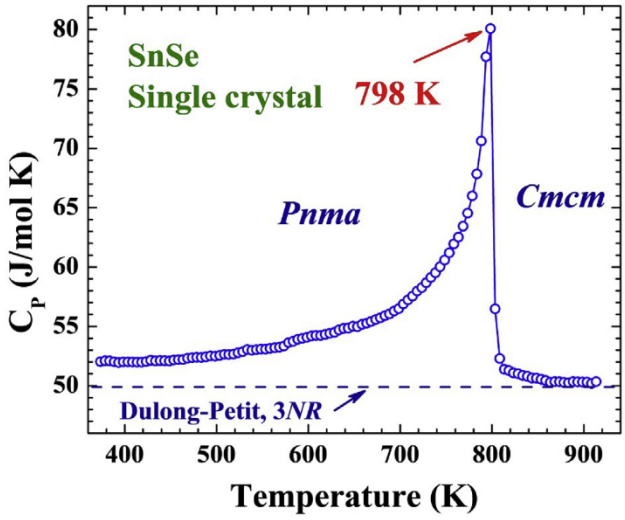


**Fig. 2. Structural transition.** Temperature dependence of heat capacity of the SnSe crystal, revealing a structural phase transition at 798 K for the crystal, where specific heat reaches 1.6 times of the Dulong-Petit limit indicated by the dashed line.

suggested that the low lattice thermal conductivity of SnSe in the *Cmcm* phase is due to anharmonic damping of the low-frequency phonon modes arising from enhanced three-phonon scattering [22,23,25]. Polarized Raman scattering suggested that anharmonicity is driven by soft optical modes [26]. To address this question we have carried out detailed high temperature inelastic neutron scattering (INS) measurements on a large single crystal (weighted 27.4 g, Fig. 1(b)) to provide direct information about the phonon dispersion relations and lifetime, focusing on the *Cmcm* phase. We find large departures of phonon dispersions from the harmonic frequencies, strong lattice anharmonicity, strong electron-phonon scattering of high-frequency phonons, phonon softening, and lifetime shortening that are all clearly revealed. The anharmonic phonon dispersions can be described using a wavevector cubed ($q^3$) dependency, which can be linked to a strong three-phonon scattering interaction. The interaction resulting downturns in the phonon dispersion at large wave vectors can be described using a wavevector square ($q^2$) dependency, with an electron effective mass that is about 625 times that of the free electron, reflecting the appearance of enhanced electron-lattice couplings in the *Cmcm* phase. Reductions in the group velocity can reach as large as 37% and the phonon lifetimes fall into the range of 0.3 ps upon thermal evolution from the *Pnma* into the *Cmcm* phase.

## 2. Results

### 2.1. Structural transition

The signature of the displacive phase transition from the *Pnma* to the *Cmcm* phase of the crystal is marked by a sharp peak at 798 K in the temperature dependence of the specific heat $C_P$ (Fig. 2). This $C_P(T)$ was measured on a small piece of crystal (~0.7 mm thick) cleaved from the edge of the same crystal shown in Fig. 1(b). Specific heat was recorded in a warming process, in steps of 5 K and a 3 min wait after the temperature was stabilized. $C_P$ departs from the Dulong-Petit limit but increases substantially with increasing temperature from well below the transition temperature, signifying the existence of a huge lattice anharmonicity in the *Pnma* phase. No thermal hysteresis of the specific heat was observed under temperature cycles in the transition regime, indicative of a second-order phase transition for the structural change. Similar thermal behavior of $C_P$ has been observed in several separate studies [27–30].

### 2.2. Phono dispersion

Neutron diffraction measurements reveal lattice constants of $a = 4.319\ (1)$ Å (Fig. 3(a)), $b = 11.721\ (3)$ Å (Fig. 3(b)) and $c = 4.305\ (1)$ Å (Fig. 3(c)) at 808 K, revealing an orthorhombic structure for the present crystal. The crystal remains in the orthorhombic phase even at 823 K with $a = 4.321\ (1)$ Å, $b = 11.731\ (3)$ Å and $c = 4.309\ (2)$ Å. To avoid melting of the crystal when is maintained at a high temperature for a long period of time for INS measurements, the phonon dispersions were measured at 808 K in the orthorhombic phase of the crystal [31]. At 808 K the value of $C_P$ has dropped 95% from its peak value associated with the transition, but is still below the transition is fully through to a tetragonal phase (Fig. 2). INS measurements allow extraction of the phonon lifetime $\tau$, where $\tau$ is related to the full-width-at-half-maximum W of the intrinsic excitation profile as $\tau = (\pi \cdot W)^{-1}$ with $\tau$ in units of ps and W in THz [32]. We denote the neutron wavevector transfer $\mathbf{Q}$ $(Q_hQ_kQ_l) = \mathbf{G}$ $(hkl) + \mathbf{q}$ (HKL), where $\mathbf{G}$ is a reciprocal lattice vector and $\mathbf{q}$ the phonon wavevector. Note that the allowed reflections in the orthorhombic *Cmcm* space group (space group No. 63) are restricted so that $h + k$ is an even integer for general $(hkl)$ reflections and $l$ is an even integer for $(h0l)$ reflections.

Fig. 4 shows several phonon groups observed in constant-Q scans. Fig. 4(a) for $\mathbf{Q} = (002) + (00L)$ reveals a phonon excitation at E = 3.32 meV for L = 0.1, with a peak width that is about twice the instrumental resolution reflecting a short lifetime for this longitudinal acoustic (LA) phonon propagating along the *c*-axis direction (filled triangles). This LA branch shifts to a higher energy at a higher $\mathbf{q}$ with a much shorter lifetime (Fig. 4(a)), with the peak width becoming ten times as large as the instrumental resolution at L = 0.8, corresponding to a very short lifetime of 0.32 ps (open circles in Fig. 4(a)). These very short phonon lifetimes directly link to the low thermal conductivity observed in the *Cmcm* phase. On the other hand, the phonon energy and lifetime depend less on $\mathbf{q}$ in approaching the zone boundary, as can be seen in the constant-Q longitudinal scans at $\mathbf{Q} = (040) + (0K0)$ (Fig. 4(b)). This branch of LA phonon exhibits less dispersion, with the phonon energy reaching only 7.3 meV with a lifetime of 0.82 ps at the zone

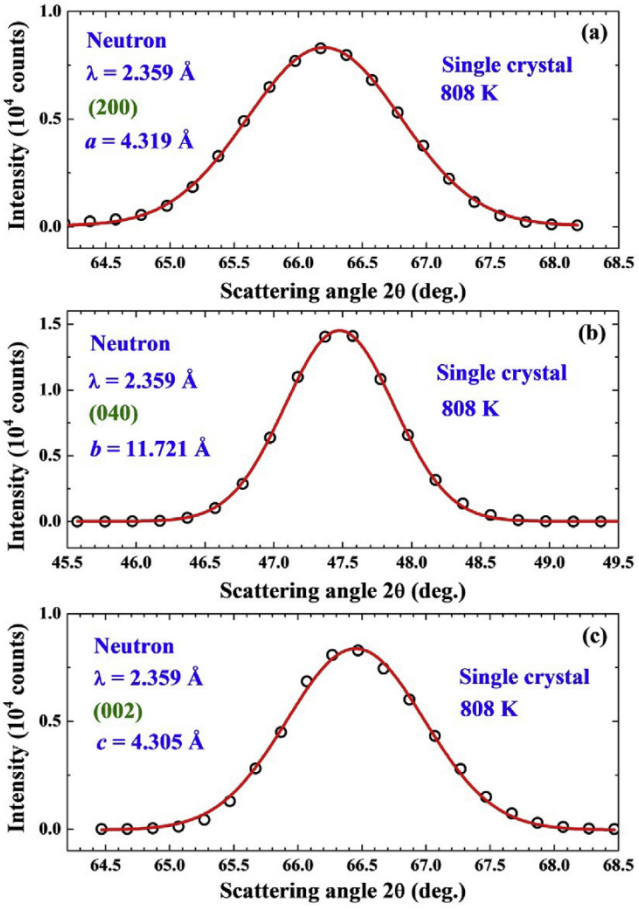


**Fig. 3. Lattice constants at 808 K.** Diffraction scans of the SnSe crystal at 808 K through (a) (200), (b) (040), and (c) (002) reflections, revealing a single Gaussian profile (solid line) for each reflection and an orthorhombic structure of $a = 4.319\ (1)$ Å, $b = 11.721\ (3)$ Å, and $c = 4.305\ (1)$ Å for the crystal at 808 K.

boundary (open circles in Fig. 4(b)). Significant reductions of the phonon energy on approaching the zone boundary are also found. The constant-Q transverse scans at $\mathbf{Q} = (002) + (H00)$ reveal a phonon energy of 4.34 meV at H = 0.3, which increases to 6.28 meV at H = 0.5, then decreases to 3.88 meV at H = 0.9 (Fig. 4(c)), revealing the appearance of giant phonon directional anharmonicty in the *Cmcm* phase.

Fig. 5 displays six phonon dispersion maps measured at 808 K, covering the entire Brillouin zone. For a direct comparison, the calculated phonon modes reported in Ref. 25 associated with the measured branches are reproduced as dashed curves. The LA phonons in the [00L] direction are much lower in energy than the calculated ones (20% smaller at the zone boundary, for example) (Fig. 5(a)). The most distinct feature seen is the appearance of a downturn in the energy dispersion along specific directions, when the phonon wavevector reaches about half way to the zone boundary (Fig. 5(c) and (d)). This downturn in phonon energy has been suggested in the calculations [25] for the phonons propagating in the [20L] direction (dashed curves in Fig. 5(c)). The observed dramatic softening of the phonon energy at the zone boundary is 45%, while the calculations only predict 11%. It is thus likely that a mechanism other than the three-phonon scattering suggested in Ref. 25 plays a dominant role in the anharmonic phonon dispersions in the *Cmcm* phase. We note that either negligible or much less softening (downturn) in the phonon dispersion is visible for the TA mode in the [04L] and LA mode in the [0K0] directions (Fig. 5(e) and (f)).

Departures of the phonon vibrations from the harmonic frequency become larger at larger wavevectors upon shifting from the zone center toward the boundary (Fig. 6(a)-(c)). The large reductions in phonon energy from the expected harmonic dispersions at large wavevectors reveal the existence of an interaction that scatters and absorbs phonon. Taking a $q^n$-dependency for this interaction, with the exponent $n$ a fitting parameter, gives $n$ ranging from 1.94 to 1.98 for the six dispersions observed. It appears that the energy associated with the interaction can be described by a $q^2$-dependency. In addition, the energy softening rate with increasing wavevector becomes smaller on approaching the zone boundary. A component of interaction that compensates the reduction of phonon energy is needed in describing the observed energy dispersions near the zone boundary. This component introduces an anharmonic term to the lattice vibrations. Apparently, a $q^m$-dependency with $m > 2$ is needed for this anharmonic term. We find that including an additional $q^4$-dependency gave a negligible coefficient for this $q^4$ term, showing the lattice anharmonicity can be described by a $q^3$-dependency. The solid curves in Fig. 6(a)-(c) show fits of the data to $E(q) = [E_h \sin(2q/\pi) + E_a q^3] - E_{e\text{-}p} q^2$, where $q$ is the wavevector in dimensionless reciprocal lattice units (r.l.u.), while $E_h$, $E_a$ and $E_{e\text{-}p}$ are the harmonic, anharmonic and scattering energies at the zone boundary, respectively. All six phonon dispersions observed can be satisfactorily described throughout the entire Brillouin zone by including this additional term (solid curves in Fig. 6(a)-(c)). In particular, note that the phonon energies at large wavevectors cannot be satisfactorily described when assuming $E(q) = E_h \sin(2q/\pi) - E_{e\text{-}p} q^n$, with $n = 1$ or 3 (Supplementary data, Figs. S1 and S2). The energy parameters obtained from the fits are listed in Table 1.

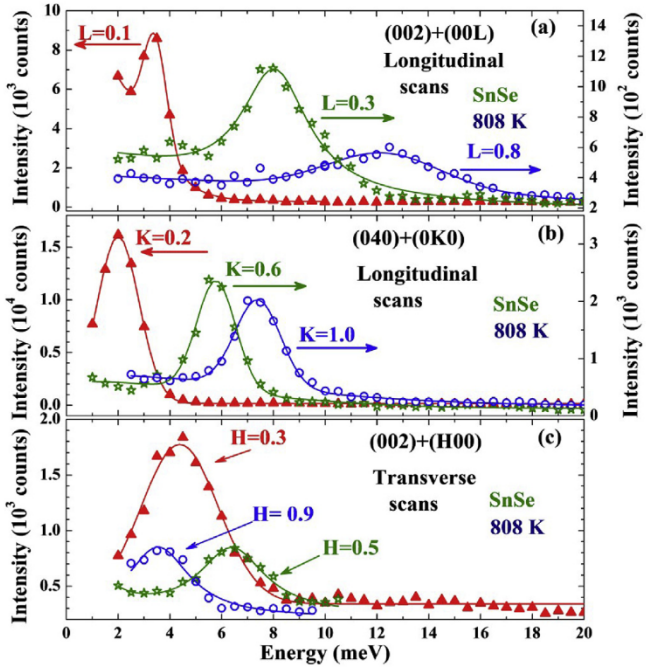


**Fig. 4. Phonon excitation spectra.** Phonon Inelastic neutron scattering constant-Q spectra at the representative wavevectors for the single crystal SnSe at 808 K, measured in (a) longitudinal scans along [00L], (b) longitudinal scans along [0K0], and (c) transverse scans along [H00].

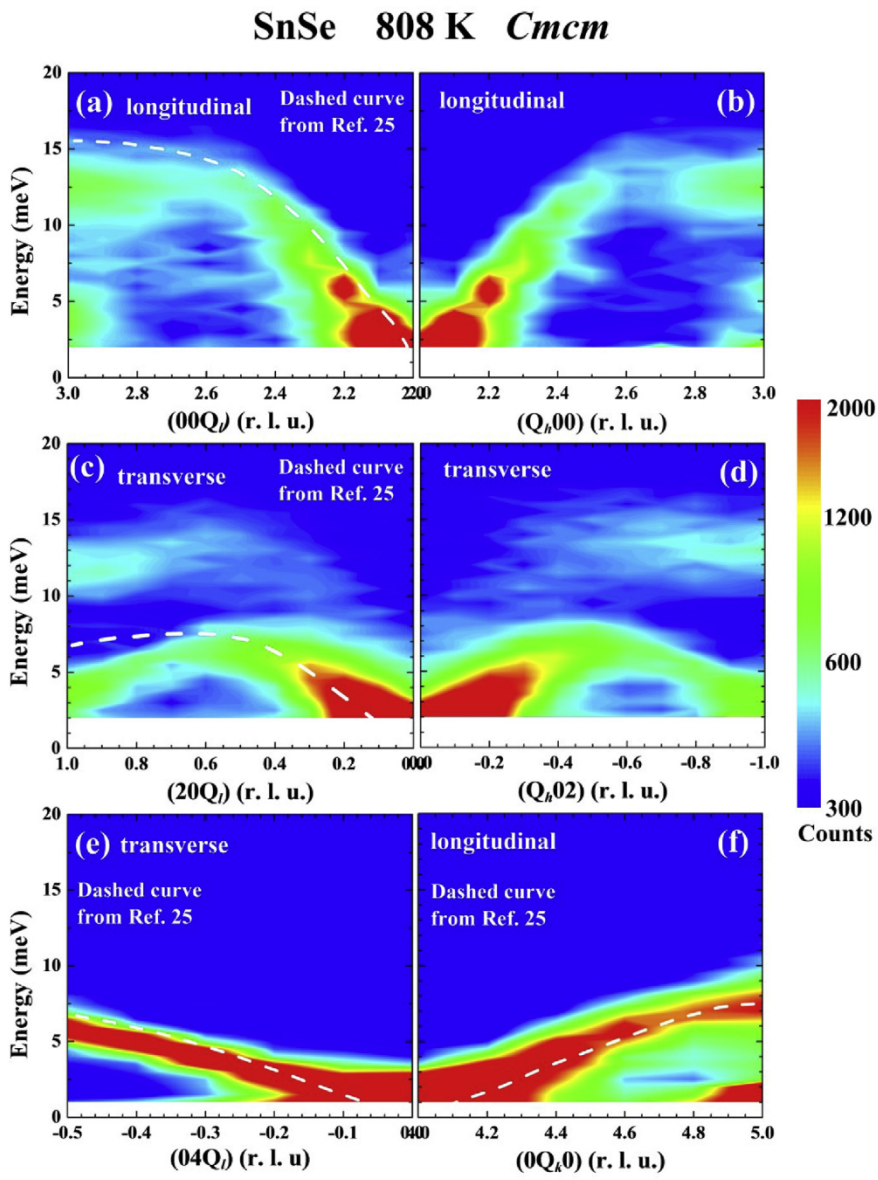


**Fig. 5. Phonon dispersion maps in the *Cmcm* phase.** Phonon excitation maps of SnSe at 808 K, measured in (a) longitudinal scans along [00$Q_l$], (b) longitudinal scans along [$Q_h$00], (c) transverse scans along [20$Q_l$], (d) transverse scans along [$Q_h$02], (e) transverse scans along [04$Q_l$], and (f) longitudinal scans along [0$Q_k$0]. The dashed curves are reproductions of the data reported in Ref. 25.

### 2.3. Phonon lifetime and propagation length

The widths of the phonon energy profiles in the INS spectra are much broader than the instrumental resolution, revealing short propagation lifetimes for the phonons in all six branches observed. Phonons with lifetimes on the order of ~0.5 ps were found, with much shorter lifetimes for phonons at larger wave vectors seen in four of the six high-symmetry branches measured (Fig. 6(d)-(f)), in particular for the LA phonons propagating along the in-plane *a*- and *c*-axis directions. The lifetimes of the $LA_a$ phonons (open squares in Fig. 6(d)) and $LA_c$ phonons (open triangles in Fig. 6(f)) were shorter by as much as ~70% upon increasing *q* from the zone center to the boundary. On the other hand, the lifetime of the in-plane TA phonons remained at ~0.5 ps throughout the Brillouin zone (open triangles in Fig. 6(d) and open squares in Fig. 6(f)). Less phonon anharmonicity and scattering was observed for the phonons propagating along the interlayer axial direction, but the phonons in these branches ($LA_b$ and $TA_b$) displayed large reductions in the lifetimes, as large as 80%, upon increasing *q* from the zone center to the boundary (open circles in Fig. 6(e) and (f)). Generally speaking, the observed phonon lifetimes at 808 K are on the order of 0.5 ps, which is a factor of ~4 shorter than the calculated ones [25] for the *Cmcm* phase at 800 K, and two orders-of-magnitude shorter than the calculated ones for the *Pnma* phase at 300 K.

Given these large linewidths, the propagation of phonons in the *Cmcm* phase only extends over several unit cells even for acoustic phonons propagating near the zone center where the group velocities are the highest (Fig. 7(a)-(c)). The phonon propagation lengths along the axial *b*-axis direction (open circles in Fig. 7(b) and (c)), on the other hand, are significantly longer than those in the basal *a*-*c* plane (open squares and triangles in Fig. 7(a) and (c)). Short phonon propagation lengths limit heat transport, which gives rise to the desired poor thermal conductivity. For the axial direction, the longer phonon propagation lengths compensate for the

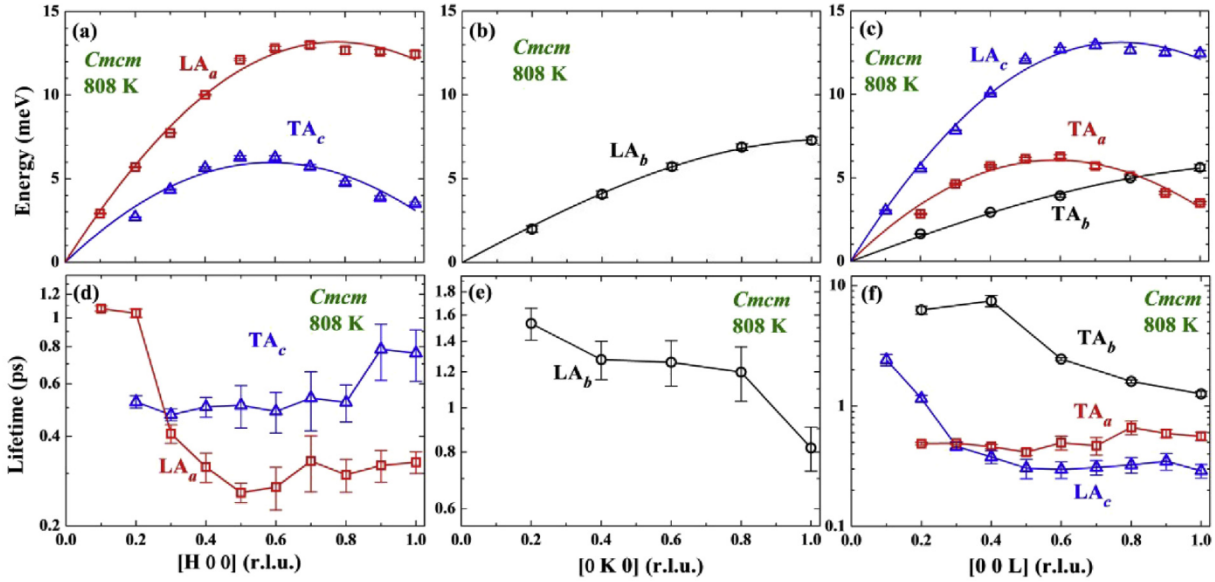


**Fig. 6. Phonon dispersions and lifetimes.** (a)–(c) Phonon dispersion curves of SnSe at 808 K along the three crystallographic directions. The solid curves indicate the results of the fits of the data to a harmonic term plus a scattering $q^2$-term plus an anharmonic $q^3$-term as discussed in the text. (d)–(f) Variations of phonon lifetimes with wavevector across the whole Brillouin zone along the three crystallographic directions.

**Table 1**
**Energy parameters in phonon dispersions.** Energy parameters obtained from fits of the observed phonon energy dispersion at 808 K.

SnSe, T = 808 K, $E(q) = [E_h \sin(\pi/2q) + E_a q^3] - E_{e\text{-}p} q^2$

| Direction | | $E_h$ (meV) | $E_a$ (meV) | $E_{e\text{-}p}$ (meV) | $E_a/E_h$ | $E_{e\text{-}p}/(E_h + E_a)$ | $m^*(m_e)$ |
|---|---|---|---|---|---|---|---|
| [H00] | LA$_a$ | 20.4 (7) | 4.6 (3) | 12.9 (6) | 23% | 52% | 623 |
| | TA$_c$ | 12.5 (7) | 3.5 (4) | 12.8 (6) | 28% | 80% | 628 |
| [0K0] | LA$_b$ | 6.9 (1) | 0.4 (1) | 0.03 (2) | 6% | 0.4% | 7097 |
| [00L] | TA$_a$ | 12.8 (6) | 3.8 (3) | 12.8 (5) | 30% | 77% | 623 |
| | TA$_b$ | 5.1 (4) | 0.4 (1) | 0.06 (2) | 7% | 1% | 33717 |
| | LA$_c$ | 19.9 (6) | 4.9 (4) | 12.9 (5) | 25% | 52% | 627 |

$m^*$: effective mass of electron-phonon coupling.
$m_e$: free electron mass.

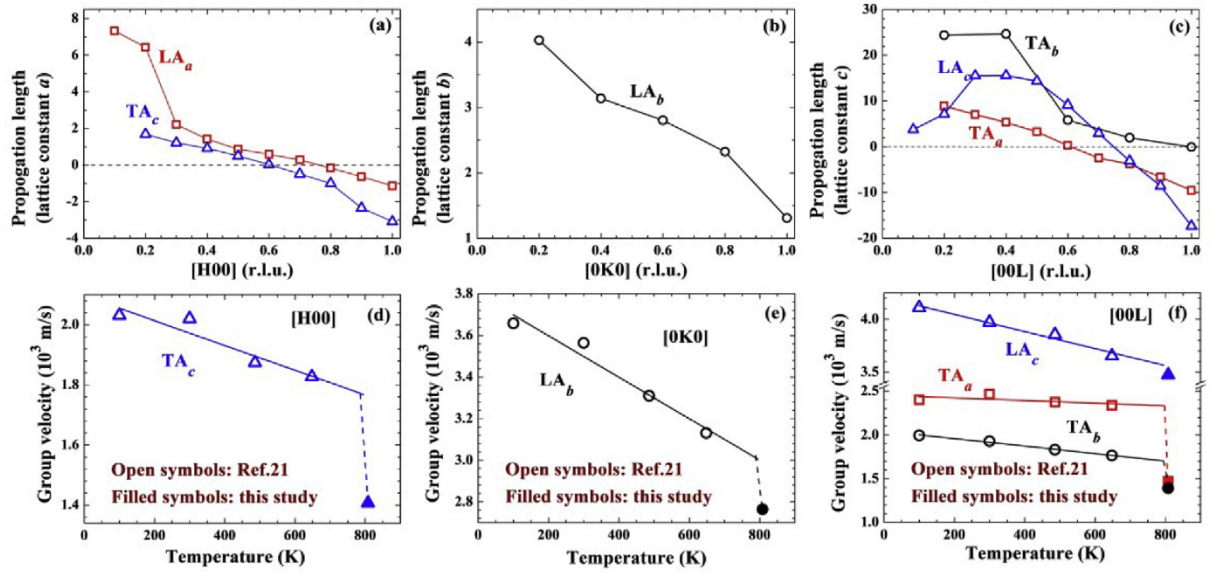


**Fig. 7. Phonon propagation lengths and group velocities.** Variation in the phonon propagation length with wavevector across the Brillouin zone for the (a) LA$_a$ and TA$_c$ modes along the *a*-axis direction, (b) LA$_b$ mode along the *b*-axis direction, and (c) TA$_a$, TA$_b$ and LA$_c$ modes along the *c*-axis direction. Direction comparisons of the phonon group velocity in the *Pnma* phase (open symbols, reported in Ref. 21) and in the high temperature *Cmcm* (filled symbols, this study) phase for the phonon modes in the (d) [H00] direction, (e) [0K0] direction, (f) [00L] direction.

very low electrical conductivity, yielding a comparable thermal conductivity [6]. Large reductions in the phonon group velocities upon transitioning from the *Pnma* to *Cmcm* phase are seen for the TA modes (Fig. 7(d)-(f)). The reduction can be as high as 40% for the $TA_a$ mode and 20% for the $TA_b$ and $TA_c$ modes, while the reductions for the LA modes are much smaller.

## 3. Discussion

Four of the six phonon branches reveal huge lattice anharmonicity and large contributions from scattering. Huge lattice anharmonicity and scattering appear primarily in the vibrations along the basal *a*- and *c*-axis directions, and much smaller in magnitude for those along the axial *b*-axis. The scattering energy $E_{e\text{-}p}$ of the in-plane transverse modes ($TA_c$ mode in [H00] and $TA_a$ mode in [00L]) reach as large as 80% of the phonon energy $E_h + E_a$; a smaller $E_{e\text{-}p}$ can be seen for the longitudinal modes, but it still reaches ~50% of $E_h + E_a$. Phonon softening from the scattering covers the entire Brillouin zone, with values that are much larger than the anharmonicity from enhanced three-phonon scattering reported in Ref. 25. Clearly, mechanisms stronger than phonon-phonon interaction play a crucial role. It is known that a $q^2$-dependency is a characteristic of the conduction-electron energy, and hence we conclude that this demonstrates there is a strong electron-phonon interaction in the *Cmcm* phase. The much stronger in-plane (*a*-*c* plane) scattering than in the axial (*b*-axis) direction can be readily understood because the in-plane electric conductivity is an order-of-magnitude higher [6].

The electron-phonon coupling strength can be expressed in term of the effective mass $m^*$ of the electron by $E_{e\text{-}p} = \hbar^2 q^2/2\ m^*$, with the $m^*$ expressed in unit of free electron mass $m_e$ for the six phonon branches measured listed in Table 1. The effective masses of the electron-phonon coupling are ~625 times that of the free electron mass for the coupling in the basal *a*-*c* plane, while those along the axial *b*-axis direction are ~50 times higher because of the poor electrical conductivity between layers. The dimensionless electron-phonon coupling constant $\alpha$ for quasi-two-dimensional SnSe [33] may then be calculated [34] by $m^*/m_e = 0.73\alpha^4$ to give $\alpha = 5.41$ for $m^* = 625\ m_e$. Increases in carrier concentration from the creation of additional Sn vacancies during the transition from the *Pnma* to the *Cmcm* phase has been reported [35]. Band gap $E_g$ narrowing from the *Pnma* phase ($E_g$ ~ 0.61 eV) to the *Cmcm* phase ($E_g$ ~ 0.39 eV) has also been reported [17]. The appearance of strong electron-phonon coupling links directly to the feasibility of effectively creates electron-hole pairs from the much narrower band gap in the *Cmcm* phase. The electron-phonon interaction can be a source for the higher carrier concentration in the *Cmcm* phase than in the *Pnma* phase.

Orbitally driven phonon anharmonicity arises from bond instability which has been reported to generate giant anharmonicity in the *Pnma* phase [21]. Lattice anharmonicity in the *Cmcm* phase from enhanced three-phonon scattering has also been reported [25]. The calculated dispersions from enhanced three-phonon scattering can be described by a harmonic frequency plus a $q^3$-dependency (Supplementary data, Fig. S3). Likely, the $q^3$-term deduced from the measured dispersions is directly related to the lattice anharmonicity, which modifies by ~25% of phonon energy compared to the harmonic terms at the zone boundary along the basal *a*- and *c*-axis directions, but considerably less in magnitude for those along the axial *b*-axis (Table 1). Downturns in phonon dispersions at large wave vectors, but with a smaller energy reduction rate, have also been observed in the *Pnma* phase at 300 K, which have been attributed to be from the low-lying optical phonon [21]. No sign for the appearance of optical branches that can be identified in the *Cmcm* phase at 808 K with energy up to 20 meV (Fig. 5). The large differences between the phonon dispersions at 300 and 808 K reflect the large difference in the thermal behavior of lattice thermal conductivity in the *Pnma* and *Cmcm* phases of SnSe [6].

## 4. Conclusions

Inelastic neutron scattering measurements performed on a large SnSe single crystal in the *Cmcm* phase at 808 K reveal a huge lattice anharmonicity as well as a strong electron-phonon scattering. The strong electron-phonon scattering causes a strong softening of the phonon energies, short lifetimes, and gives rise to negative group velocities for large wavevectors for phonons propagating in the crystallographic basal planes. The very short phonon lifetimes are the origin of the low thermal conductivity observed at high temperatures. The very limited phonon propagation length together with negative phonon group velocity at large wavevectors restricts heat transport, which explains the origin of the poor thermal transport as a result of a strong electron-phonon scattering in the high temperature *Cmcm* phase of SnSe.

## 5. Materials and methods

### 5.1. Preparation of SnSe single crystals

Single crystals of SnSe were grown using the vertical Bridgman method, employing a growth temperature of 1223 K and a growth rate of 1.5 mm/h. High purity Sn chunks and Se shots (both 99.999% pure) were weighed in the stoichiometric ratio of SnSe, sealed in evacuated silica tubes, heated at 1223 K for 48 h, followed by furnace-cooling to room temperature. The cylindrical single crystal (12.6 mm in diameter and 35.9 mm in length) used in the present measurements weighted 27.4 g (Fig. 1(b)), and was cleaved along the basal *a*-*c* plane to yield flat surfaces that exhibited a metallic luster. A mass density of 6.14 g/cm$^3$ was obtained for the crystal at room temperature, which agrees well with the theoretical value.

### 5.2. Inelastic neutron scattering

Single crystal neutron scattering measurements were conducted at the NIST Center for Neutron Research, using the BT-7 triple-axis spectrometer with energy of neutrons defined by pyrolytic graphite (PG) (002) crystals at both the monochromator and analyzer positions, using a fixed final energy of 14.7 meV with PG filter to suppress higher order contaminations [36]. The sample temperature was controlled using the F-BNL furnace system, allowing the sample to be in a helium gas atmosphere (SnSe melts at a considerably lower temperature in a vacuum). A slow heating rate of 5 K/min below 700 K and 2 K/min above was employed to avoid possible sample breakage from different thermal expansion rates in the three crystal axis directions. The single crystal was mounted to allow access to the *a*-*c* or *b*-*c* crystallographic planes for an overview of the *h*-*k*-*l* reciprocal space scattering intensity survey.

## Author contributions

W.H.L., C.H.L., Y.Z. designed the study; C.H.L., M.H.M., Y.Z., W.H.L., J.W.L. performed the measurements; C.H.L., M.H.M., W.H.L. analyze the data; P.C.W. and Y.Y.C. fabricate the samples; all of the authors discussed the results; W.H.L. and J.W.L. wrote the manuscript.

## Funding

This work was supported by the Ministry of Science and Technology of Taiwan under Grant No. MOST 107-2112-M-008-026-MY2.

## Declaration of competing interest

The authors declare that they have no competing interests.

## Acknowledgments

We thank Juscelino Leao of NIST for his assistance with the furnace.

## Appendix A. Supplementary data

Supplementary data to this article can be found online at https://doi.org/10.1016/j.mtphys.2019.100171.

## References

[1] G.J. Tan, L.-D. Zhao, M.G. Kanatzidis, Rationally designing high-performance bulk thermoelectric materials, Chem. Rev. 116 (2016) 12123.
[2] L.E. Bell, Cooling, heating, generating power, and recovering waste heat with thermoelectric systems, Science 321 (2008) 1457.
[3] L.D. Zhao, V.P. Dravid, M.G. Kanatzidis, The panoscopic approach to high performance thermoelectrics, Energy Environ. Sci. 7 (2014) 251.
[4] J.R. Sootsman, D.Y. Chung, M.G. Kanatzidi, New and old concepts in thermoelectric materials, Angew. Chem. Int. Ed. 48 (2009) 8616.
[5] M.S. Dresselhaus, G. Chen, M.Y. Tang, R.G. Yang, H. Lee, D.Z. Wang, Z.F. Ren, J.-P. Fleurial, P. Gogna, New directions for low-dimensional thermoelectric materials, Adv. Mater. 19 (2007) 1043.
[6] L.-D. Zhao, S.-H. Lo, Y. Zhang, H. Sun, G. Tan, C. Uher, C. Wolverton, V.P. Dravid, M.G. Kanatzidis, Ultralow thermal conductivity and high thermoelectric figure of merit in SnSe crystals, Nature 508 (2014) 373.
[7] L.-D. Zhao, G. Tan, S. Hao, J. He, Y. Pei, H. Chi, H. Wang, S. Gong, H. Xu, V.P. Dravid, C. Uher, G.J. Snyder, C. Wolverton, M.G. Kanatzidis, Ultrahigh power factor and thermoelectric performance in hole-doped single-crystal SnSe, Sicence 351 (2016) 141.
[8] A.T. Duong, V.Q. Nguyen, G. Duvjir, V.T. Duong, S. Kwon, J.Y. Song, J.K. Lee, J.E. Lee, S. Park, T. Min, J. Lee, J. Kim, S. Cho, Achieving ZT=2.2 with Bi-doped n-type SnSe single crystals, Nat. Commun. 7 (2016) 13713.
[9] Y. Zhang, S. Hao, L.-D. Zhao, C. Wolvertonc, Z. Zeng, Pressure induced thermoelectric enhancement in SnSe crystals, J. Mater. Chem. 4 (2016) 12073.
[10] Z.-G. Chen, X. Shi, L.-D. Zhao, J. Zou, High-performance SnSe thermoelectric materials: progress and future challenge, Prog. Mater. Sci. 97 (2018) 283.
[11] W. Shi, M. Gao, J. Wei, Ji Gao, C. Fan, E. Ashalley, H. Li, Z. Wang, Tin selenide (SnSe): growth, properties, and applications, Adv. Sci. 5 (2018) 1700602.
[12] P.-C. Wei, S. Bhattacharya, J. He, S. Neeleshwar, R. Podila, Y.Y. Chen, A.M. Rao, The intrinsic thermal conductivity of SnSe, Nature 539 (2016) E1–E2.
[13] S. Wang, S. Hui, K. Peng, T.P. Bailey, W. Liu, Y. Yan, X. Zhou, X. Tang, C. Uher, Low temperature thermoelectric properties of p-type doped single-crystalline SnSe, Appl. Phys. Lett. 112 (2018) 142102.
[14] Z. Nabi, A. Kellou, S. Mecabih, A. Khalfi, N. Benosman, Opto-electronic properties of rutile SnO2 and orthorhombic SnS and SnSe compounds, Mater. Sci. Eng. B 98 (2003) 104.
[15] M. Taniguchi, R.L. Johnson, J. Ghijsen, M. Cardona, Core excitons and conduction-band structures in orthorhombic GeS, GeSe, SnS, and SnSe single crystals, Phys. Rev. B 42 (1990) 3634.
[16] M. Sist, J. Zhang, B.B. Iversen, Crystal structure and phase transition of thermoelectric SnSe, Acta Crystallogr. B 72 (2016) 310.
[17] L.-D. Zhao, C. Chang, G. Tanb, M.G. Kanatzidis, SnSe: a remarkable new thermoelectric material, Energy Environ. Sci. 9 (2016) 3044.
[18] T. Chattopadhyay, J. Pannetier, H.G. von Schnering, Neutron diffraction study of the structural phase transition in SnS and SnSe, J. Phys. Chem. Solids 47 (1986) 879.
[19] Y. Xiao, C. Chang, Y. Pei, D. Wu, K. Peng, X. Zhou, S. Gong, J. He, Y. Zhang, Z. Zeng, L.-D. Zhao, Origin of low thermal conductivity in SnSe, Phys. Rev. B 94 (2016) 125203.
[20] J. Carrete, N. Mingo1, S. Curtarolo, Low thermal conductivity and triaxial phononic anisotropy of SnSe, Appl. Phys. Lett. 105 (2014), 101907.
[21] C.W. Li, J. Hong, A.F. May, D. Bansal, S. Chi, T. Hong, G. Ehlers, O. Delaire, Orbitally driven giant phonon anharmonicity in SnSe, Nat. Phys. 11 (2015) 1063.
[22] D. Bansal, J. Hong, C.W. Li, A.F. May, W. Porter, M.Y. Hu, D.L. Abernathy, O. Delaire, Phonon anharmonicity and negative thermal expansion in SnSe, Phys. Rev. B 94 (2016), 054307.
[23] C. Chang, L.-D. Zhao, Anharmoncity and low thermal conductivity in thermoelectrics, Materials Today Physics 4 (2018) 50.
[24] B. Xu, J. Zhang, G. Yu, S. Ma, Y. Wang, L. Yi, Comparative study of electronic structure and thermoelectric properties of SnSe for Pnma and Cmcm phase, J. Electron. Mater. 45 (2016) 5232.
[25] J.M. Skelton, L.A. Burton, S.C. Parker, A. Walsh, C.-E. Kim, A. Soon, J. Buckeridge, A.A. Sokol, C.R.A. Catlow, A. Togo, I. Tanaka, Anharmonicity in the high-temperature Cmcm phase of SnSe: soft modes and three-phonon interactions, Phys. Rev. Lett. 117 (2016), 075502.
[26] F. Liu, P. Parajuli, R. Rao, P.C. Wei, A. Karunarathne, S. Bhattacharya, R. Podila, J. He, B. Maruyama, G. Priyadarshan, J.R. Gladden, Y.Y. Chen, A.M. Rao, Phonon anharmonicity in single-crystalline SnSe, Phys. Rev. B 98 (2018) 224309.
[27] S. Sassi, C. Candolfi, J.-B. Vaney, V. Ohorodniichuk, P. Masschelein, A. Dauscher, B. Lenoir, Assessment of the thermoelectric performance of polycrystalline p-type SnSe, Appl. Phys. Lett. 104 (2014) 212105.
[28] Q. Zhang, E.K. Chere, J. Sun, F. Cao, K. Dahal, S. Chen, G. Chen, Z. Ren, Studies on thermoelectric properties of n-type polycrystalline $SnSe_{1-x}S_x$ by iodine doping, Adv. Energy Mater. 5 (2015), 1500360.
[29] P.-C. Wei, S. Bhattacharya, Y.-F. Liu, F. Liu, J. He, Y.-H. Tung, C.-C. Yang, C.-R. Hsing, D.-L. Nguyen, C.-M. Wei, M.-Y. Chou, Y.-C. Lai, T.-L. Hung, S.-Y. Guan, C.-S. Chang, H.-J. Wu, C.-H. Lee, W.-H. Li, R.P. Hermann, Y.-Y. Chen, A.M. Rao, Thermoelectric figure-of-merit of fully dense single-crystalline SnSe, ACS Omega 4 (2019) 5442.
[30] U. Aseginolaza, R. Bianco, L. Monacelli, L. Paulatto, M. Calandra, F. Mauri, A. Bergara, I. Errea, Phonon collapse and second-order phase transition in thermoelectric SnSe, Phys. Rev. Lett. 122 (2019), 075901.
[31] A Crystal Similar to the Present One Melted after Stayed at 823 K for 5 Days of INS Measurements.
[32] G. Nilsson, G. Nelin, Phonon dispersion relations in Ge at 80 K, Phys. Rev. B 3 (1971) 364.
[33] V. Tayari, B.V. Senkovskiy, D. Rybkovskiy, N. Ehlen, A. Fedorov, C.-Y. Chen, J. Avila, M. Asensio, A. Perucchi, P. di Pietro, L. Yashina, I. Fakih, N. Hemsworth, M. Petrescu, G. Gervais, A. Grüneis, T. Szkopek, Quasi-two-dimensional thermoelectricity in SnSe, Phys. Rev. B 97 (2018), 045424.
[34] C. Grimaldi, Weak-and strong-coupling limits of the two-dimensional Fröhlich polaron with spin-orbit Rashba interaction, Phys. Rev. B 77 (2008), 024306.
[35] A. Dewandre, O. Hellman, S. Bhattacharya, A.H. Romero, G.K.H. Madsen, M.J. Verstraete, Two-step phase transition in SnSe and the origins of its high power factor from first principles, Phys. Rev. Lett. 117 (2016) 276601.
[36] J.W. Lynn, Y. Chen, S. Chang, Y. Zhao, S. Chi, W. Ratcliff, B.G. Ueland, R.W. Erwin, Double-focusing thermal triple-Axis spectrometer at the NCNR, J. Res. NIST 117 (2012) 61.